

pubs.acs.org/Macromolecules Article

# Shape Anisotropy Enhances Nanoparticle Dynamics in Nearly Homogeneous Hydrogels

Katie A. Rose, Natalie Gogotsi, Jonathan H. Galarraga, Jason A. Burdick, Christopher B. Murray, Daeyeon Lee,\* and Russell J. Composto\*



Cite This: Macromolecules 2022, 55, 8514-8523



ACCESS More Article Recommendations Supporting Information

Gelation Time

**ABSTRACT:** Single particle tracking is used to investigate the effect of nanoparticle shape anisotropy on dynamics. The mean squared displacements of poly(ethylene glycol) (PEG)-functionalized quantum dot (QD) and quantum rod (QR) probes of similar diameters are examined during the gelation of a tetra-poly(ethylene glycol) (tetra-PEG) hydrogel. At early times prior to the gel time  $(t_{\rm gel})$ , QDs exhibit greater mobility than their QR counterparts. However, as gelation proceeds, QRs exhibit increased dynamics compared to QDs, suggesting enhanced rod dynamics in increasingly confined networks. Potential mechanisms are discussed, including the influence of rotational dynamics and the increased parallel diffusion of rods in confined systems. This study provides insights into developing nanoparticle probes of different shape anisotropy, with particular importance for their use in drug delivery and other biomedical applications.

# **■ INTRODUCTION**

Understanding and controlling nanoparticle dynamics in polymeric systems is key to a variety of applications including filtration, <sup>1–5</sup> nanoparticle dispersion in composites, <sup>6–10</sup> and drug delivery <sup>11,12</sup> among others. The parameter space that governs nanoparticle dynamics in these systems is extensive and can be broadly categorized into those related to the probe itself and those related to the network. The parameters related to the probe includes the particle size compared to the characteristic length of the system, <sup>13–15</sup> the functionality of the particle which in turn determines probe-network interactions, <sup>15–21</sup> and the particle shape. <sup>22–28</sup> This study explores the effect of particle anisotropy on diffusion through a hydrogel network.

In particular, investigating the dynamics of rod shaped-particles is of interest due to the use of flexible and rigid rod particles in biomedical applications, including the tobacco mosaic virus  $(TMV)^{29-31}$  potato virus  $X^{32-34}$  and gold nanorods. Rod-shaped particles have been shown to be advantageous for several reasons: first, rod particles have a larger specific surface area compared to their spherical counterparts. By utilizing this larger area for attaching

molecules, one can achieve increased loading of drug cargo or other targeting moieties on a single particle leading to greater treatment efficacy.<sup>38</sup> In addition, it has been experimentally shown that nanorods, in comparison to spheres with similar hydrodynamic diameters or minor diameters, exhibit more rapid diffusion in mucus,<sup>39</sup> the interstitial matrix of tumors,<sup>40</sup> and agarose spheroids.<sup>41</sup> While confinement slows down the dynamics of individual particles regardless of their shape, the increased diffusion of anisotropic particles compared to similarly sized spheres has been attributed to the additional rotational component due to the anisotropic shape of the rod and increased parallel diffusion in a confining pore. For example, work by Yu et al. compares the dynamics of 80 nm spheres with rods of the same diameter, 80 × 240 nm.<sup>39</sup> In this

Received: July 29, 2022
Revised: September 12, 2022
Published: September 30, 2022





experimental system, rods are observed to have greater diffusion coefficients compared to spheres. Corresponding molecular dynamics simulations reveal that the movement of the rod is enhanced by its ability to rotate around polymer chains, allowing rod particles to more easily enter an adjacent mesh compared to a sphere of similar diameter. As a result, the spheres remain primarily caged within a single mesh, whereas on the same time scale, the rods have an increased probability of translocating to another mesh, leading to the enhanced dynamics. Additionally, these enhanced dynamics are most prominent when the mesh size is slightly larger than the length of the rod, with a decrease in the observed trend at large mesh sizes. Overall, the authors found that the rod particles exhibited a faster center of mass dynamics compared to spheres of identical diameter when the rod lengths are comparable to that of the mesh size due to the rotational dynamics of the rods.

Using bulk fluorescence intensity measurements, Lee et al. demonstrated that high aspect ratio TMV, 18 × 300 nm, exhibited increased bulk infiltration into pre-formed agarose spheroids at early times in the infiltration process compared to spherical cowpea mosaic virus (CPMV, 30 nm diameter), before a slowed second phase of infiltration.<sup>41</sup> At 5 min of infiltration, the diffusion coefficient of the TMV in the agarose spheroid is slightly larger than the diffusion coefficient in buffer. For the same infiltration time of 5 min, the dynamics of the CPMV is slowed in the agarose spheroid, with a threefold reduction in the diffusion coefficient compared to in buffer. At 30 min, the TMV undergoes a rapid decrease in dynamics, with a 12-fold reduction in the diffusion coefficient compared to in buffer, versus CMPV which only experiences a fourfold reduction. The authors attribute this biphasic diffusion behavior to the TMV orienting preferentially within the channels due to the confinement of the pores ( $\sim$ 100–700 nm) around the long axis of the rod, creating more efficient anisotropic diffusion at early times of infiltration. However, at 30 min, the rods become trapped in the pores, blocking pore access to other rod particles, resulting in an overall decrease in infiltration. Because they are spherical, the CPMV particles experience isotropic diffusion within the pores resulting in lower infiltration at early times (5 min). However, at longer times (30 min), the CPMV nanoparticles are able to infiltrate more effectively into the pores due to the lower probability of a smaller spherical particle becoming fully trapped. Overall, these two studies along with others indicate that for similar volume fractions of particles, rods have the potential to be more effective delivery systems for drug delivery and enhanced imaging applications. Studies on the dynamics of rod particles in complex media, such as mucus, provide important practical insights toward their translation. However, to systematically investigate how key length scales contribute to the observed increased dynamics of rods compared to similarly sized spheres, single particle tracking (SPT) studies in model nanoparticle and polymer matrix systems can be used to obtain additional insights and to better understand the mechanisms underlying the dynamics, as well as the interplay between anisotropic particles and their local environments.

Tetra-poly(ethylene glycol) (tetra-PEG) hydrogels, formed through the crosslinking of 4-armed tetra-PEG macromers, exhibit a nearly homogeneous network structure with few structural defects (e.g. loops and dangling chains), leading to excellent mechanical properties. While structural defects can occur in these networks, particularly at low polymer concentrations, 46,47 nearly ideal, model networks can be

formed due to the underlying structure of the tetra-PEG macromers and the reaction conditions. First, the mesh size is dictated by the molecular weight of the tetra-PEG macromer arms, which is the building block responsible for the development of a more uniform and controlled network structure. 48 Second, the end functional groups on the tetra-PEG macromers are unable to react with another arm of the same macromer, greatly suppressing the formation of loops and other higher order defects as seen in nuclear magnetic resonance (NMR) and Monte Carlo simulations.<sup>47</sup> Some examples of commonly used reactive end functional group combinations are (1) amines and N-hydroxysuccinimidylesters (NHS) and (2) maleimides and thiols; both pairs of functional groups may be prepared stoichiometrically with either two tetra-PEG macromers or one tetra-PEG macromer and a one linear-PEG. <sup>49-51</sup> Finally, for optimized reaction conditions, the gelation kinetics follows reaction-limited growth. For tetra-PEG hydrogels formed through the reaction of tetra-PEG-amine and tetra-PEG-NHS, this requires optimizing both the pH, to control the reaction rate, and the ionic strength, to control the diffusion of the tetra-PEGamine. To create a homogeneous hydrogel structure, these parameters must be tuned so that the reaction rate is fast enough that the end functional groups couple before the NHS end group of the tetra-PEG-NHS is hydrolyzed, but slow enough to allow for homogeneous mixing of the tetra-PEG macromers. For example, at high pH, too many amines on the tetra-PEG-amine are activated, resulting in pre-mature gelation prior to homogeneous mixing. Conversely, at low pH, the reaction rate is too slow such that complete gelation does not occur before the dissociation of NHS from the tetra-PEG-NHS, producing a more heterogeneous network structure. 50

As previously reported by others, the mesh size,  $\xi$ , for a fully crosslinked 20 kg/mol tetra-PEG hydrogel at c\* is on the order of a few nanometers, measured to be ~3 nm via small angle Xray scattering.<sup>53</sup> While  $\xi = 3$  nm is for the final tetra-PEG hydrogel, our previous work has shown that during the gelation process, spherical particles with a hydrodynamic diameter comparable to  $\xi$  experience different local environments at different time points of gelation.<sup>54</sup> At times prior to gelation, the nanoparticles diffuse long distances as expected since the gel is in a sol state. At long times (i.e., after the network is nearly completely formed), the particles become trapped and are immobilized within the gel. At intermediate times, the particles experience a variety of local microenvironments, leading to a wide range of dynamics. This creates a unique system to investigate how the dynamics of probe particles of different shapes evolve throughout the gelation process in response to the increasing confinement and changes in network structure.

This study seeks to understand the influence of nanoparticle anisotropy on particle dynamics as a function of increasing confinement during the gelation of a tetra-PEG hydrogel. Using SPT to resolve individual placements of nanoparticles, different populations of particle dynamics can be identified. Two types of particles are investigated: (1) PEG-functionalized quantum dots (QDs) with a diameter of 8 nm and (2) PEG-functionalized quantum rods (QRs) with a diameter × length of 9 × 23 nm. In both cases, the nanoparticles have diameters about 3 times larger than the average mesh size of the tetra-PEG hydrogel in its completely gelled state ( $\xi = 3$  nm). The macroscopic properties, including the gel time,  $t_{\rm gel}$ , are evaluated for the tetra-PEG hydrogel at the overlap

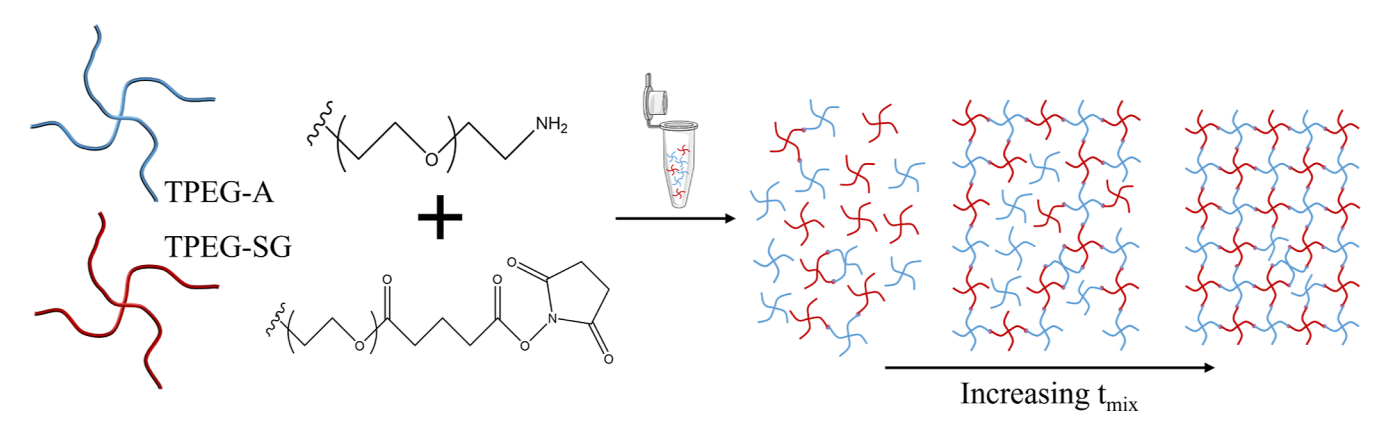


Figure 1. Reaction scheme of tetra-PEG succinimidyl glutarate (TPEG-SG, red) and amine (TPEG-A, blue) macromers (20 kg/mol, 5 kg/mol per arm). The NHS-ester (TPEG-SG) and amine (TPEG-A) react in a condensation reaction. After initial mixing, the mixture is homogeneous, but as the reaction increases, a heterogeneous network forms with regions of open network (large mesh sizes). At long times, a nearly homogeneous network forms with a few defects as shown on the far right.

concentration,  $c^*$ , to inform key time points in particle tracking. We find that at early times in gelation, before  $t_{\rm gel}$ , the mobility of the QDs is faster than that of their rod-shaped counterparts. However, close to and past  $t_{\rm gel}$ , the QRs experience faster dynamics compared to the spherical nanoparticles. The trajectories of individual QRs at times past  $t_{\rm gel}$  indicate that repeated caging and dynamic motion could explain the increased mobility. Overall, our work demonstrates the importance of probe shape anisotropy in controlling nanoparticle dynamics in systems, in which the size of the particle is comparable to the fully gelled hydrogel mesh size.

## EXPERIMENTAL SECTION

Materials. The tetra-PEG macromers, TPEG-amine (TPEG-A) and TPEG-succinimidyl glutarate (TPEG-SG), both 20 kg/mol, are purchased from JenKem. Citric acid, dibasic sodium phosphate, sodium phosphate dibasic heptahydrate, and sodium phosphate monobasic dihydrate are purchased from Sigma-Aldrich. Thiol PEG (SH-PEG), 5 kg/mol, is purchased from Creative PEGWorks. Disposable dual-sided adhesive silicone wells are purchased from Grace Biolabs.

CdSe/ZnS QDs and CdSe/CdS QRs. Oleic acid-capped CdSe/ ZnS QDs and CdSe/CdS QRs in toluene are synthesized as described previously. 55-57 The core/shell of both the QDs and QRs is measured via transmission electron microscopy (TEM) and found to be 3 nm and 4 × 18 nm, respectively (see Supporting Information). To disperse the particles in an aqueous solution and to prevent specific interactions between the probe particle and the hydrogel, the oleic acid-capped QD and QRs are chemically modified with a 5 kg/mol thiol PEG ligand as described previously. The PEG-functionalized hydrodynamic diameter of each particle type is determined by measuring their diffusion coefficient in glycerol-water solutions of known viscosity and fitting to the Stokes-Einstein equation (see Supporting Information), resulting in a hydrodynamic diameter of 8 nm for the QD. Because the PEG brush is the same for both QDs and QRs, we add 5 nm to the core/shell size of the QRs, yielding a hydrodynamic size of 9 × 23 nm and a hydrodynamic diameter of 20.5 nm. The validity of this approach is confirmed by comparing the diffusion coefficient of the PEG-functionalized QRs to the theoretical diffusion coefficient for short rods, as developed by Tirado and Garcia de la Torre (see Supporting Information).

**Tetra-PEG Hydrogel Synthesis.** Molds are prepared by adhering a silicone well to a clean #1 coverslip, pressing gently to ensure the well is fully adhered to the glass. Prior to use, each coverslip is rinsed 3 times with alternating rinses of methanol and toluene and subsequently cleaned via UV-Ozone for 10 min to remove any impurities or contaminants on the surface. TPEG-SG and TPEG-A

macromers are dissolved in phosphate buffer (50 mM, pH 7.4) and phosphate-citrate buffer (50 mM, pH 5.8), respectively, by briefly vortexing the solutions for 30 s. Due to the hydrolysis of the NHSester end functional group, the TPEG-SG macromer in solution, polymer solutions are prepared immediately prior to use. Equal amounts of each TPEG macromer solution are added to a 0.6 mL centrifuge tube,  $t_{mix} = 0$  min, before briefly mixing and immediately transferring to the prepared mold. A second clean coverslip is adhered to the top of the well to create a sealed chamber to prevent water loss from the system due to evaporation. All studies are conducted at the critical overlap concentration, c\*, which has been previously determined to be 40 mg/mL for 20 kg/mol 4-armed TPEGs.<sup>59</sup> For particle tracking studies, the initial concentration of the TPEG solutions is 45 mg/mL to account for the addition of the nanoparticle probe solution, resulting in a final polymer concentration in the gel of 40 mg/mL, or  $c^*$ .

**Tetra-PEG Hydrogel Characterization.** Rheological measurements are performed on an AR2000ex (TA Instruments) stress-controlled rheometer fitted with a steel cone (0° 59′ 42″ angle, 20 mm diameter) and plate geometry. A time sweep during polymerization is conducted (1% strain, 1 Hz) to determine the crossover of the storage, G', and loss, G'', moduli (i.e., the gel time) as well as the plateau storage modulus,  $G_p'$ . To prevent evaporation during the measurement, all experiments are conducted using a solvent trap and a constant temperature of 20 °C, corresponding to the temperature of the microscope stage in particle tracking. All samples are collected in duplicate on separate days for reproducibility with  $\pm$  indicating the standard deviation between runs. Because the sample is mixed off the rheometer and then placed on the bottom plate for the measurement, all rheological measurements start at  $t_{\rm mix} = 3$  min, which is reflected by an initial shift in the data.

**Single Particle Tracking.** Probe dynamics are imaged using an inverted Nikon Eclipse Ti optical microscope equipped with a  $100 \times$ , 1.49 NA Nikon oil immersion objective at  $20~^{\circ}$ C. Videos of a  $1200 \times 1200$  pixel region of interest are collected on a sCMOS camera (Prime-95B, Photometrics) at 33.3 frames per second. The focal plane of imaging is  $\sim 2~\mu$ m. A video acquisition time of 30 s is chosen to ensure that particle dynamics within a video are relatively consistent compared to the overall timescale of gelation. Particles are localized using a 2D Gaussian fit and linked into trajectories using Fluorescence Image Evaluation Software for Tracking and Analysis (FIESTA). To account for particles diffusing in and out of the focal plane as well as QD and QR blinking, the code allows for missing frames in order to properly link particle trajectories. Mean squared displacements (MSDs) are calculated in MATLAB using open-source code, msdanalyzer, along with custom developed code.

The MSD of a probe particle, or the square of the net distance a particle travels, is described by

$$MSD(\tau) = \langle \Delta r(\tau)^2 \rangle_t = \langle [r(t+\tau) - r(t)]^2 \rangle_t \tag{1}$$

where  $\tau$  is the lag time, r(t) is the position of the particle at absolute time t, and  $\langle \rangle_t$  denotes the averaging over time. The displacements of an individual probe's motion are determined by

$$\Delta r = \Delta x = x(\tau + \tau_i) - x(\tau), \qquad \Delta y = y(\tau + \tau_i) - y(\tau)$$
(2)

where  $\tau_i$  is the time interval between positions and  $\Delta r$  represents the displacements in both x and y.

#### RESULTS AND DISCUSSION

Using SPT, this study investigates the effect of nanoparticle shape anisotropy on the dynamics of PEG functionalized 8 nm QD spheres and 9 × 23 nm QRs during the gelation of tetra-PEG which form a nearly homogeneous network. Rheological measurements are used to characterize macroscopic changes in the gel during the gelation process, including the gel time,  $t_{\rm gel}$ . Nanoparticle dynamics are measured at various time points after mixing,  $t_{\rm mix}$ , including those before  $t_{\rm gel}$  ( $t_{\rm mix}$  = 10, 20 min) and those after  $t_{\rm gel}$  ( $t_{\rm mix}$  = 30, 60 min). During gelation, rods are observed to diffuse faster than spheres. Mechanisms for faster rod dynamics at times near and after  $t_{\rm gel}$  are discussed, focusing on the influence of rotational dynamics and increased parallel diffusion.

Tetra-PEG Hydrogel Rheology. Before measuring the dynamics of particles during gelation, the macroscopic properties of the tetra-PEG hydrogel is determined to identify the key time points during gelation for particle tracking experiments. As represented schematically in Figure 1, at early times after mixing, the TPEG-SG and TPEG-A are expected to be homogeneously distributed in solution. As gelation proceeds, the network begins to form, as the amine (TPEG-A) and the NHS-ester (TPEG-SG) groups react to create strands between the tetra-functional cores. The resulting network is heterogeneous at these intermediate time points of gelation, with regions of both low and high crosslinking density. At longer reaction times, a nearly ideal network forms with few defects and a small mesh size, dictated by the size of the tetra-PEG macromers arms. To follow the macroscopic evolution of network formation, we use oscillatory shear time sweeps spanning the reaction time to examine changes in the storage (G') and loss (G'') moduli increase after the initial mixing.

Immediately after mixing, the loss modulus is larger than the storage modulus, indicating that the solution is more fluid-like than solid (Figure 2, Table 1). However, as gelation proceeds, G' becomes larger than G''. This crossover indicates the gel time,  $t_{gel}$ , at 24 min. With this time point in mind, we focus on investigating the dynamics of the sphere and rod particles before ( $t_{\text{mix}} = 10$  and 20 min) and after ( $t_{\text{mix}} = 30$  and 60 min) the gel time to examine how particle dynamics are influenced by the evolution of the local environment. At early times of gelation,  $t_{\text{mix}} = 10$  and 20 min, the system is in a solution state, with G' < 1 Pa. Near  $t_{\rm gel}$  ( $t_{\rm mix} = 30$  min), a loosely percolated network is formed with  $G' = 34 \pm 5.5$  Pa. Near 2 times  $t_{gel}$  ( $t_{mix}$ = 60 min), G' increases by over 20 times, with G' = 670  $\pm$  1.6 Pa as the crosslinking density increases; large open regions fill in, and a more mechanically robust network forms. The network is nearly complete after 256 min (ca. 10 times the gel time) with  $G_p'=2212.0\pm54.0$  Pa. While the time for the network to fully form is long past  $t_{gel}$ , we focus on examining nanoparticle dynamics at times when the network structure

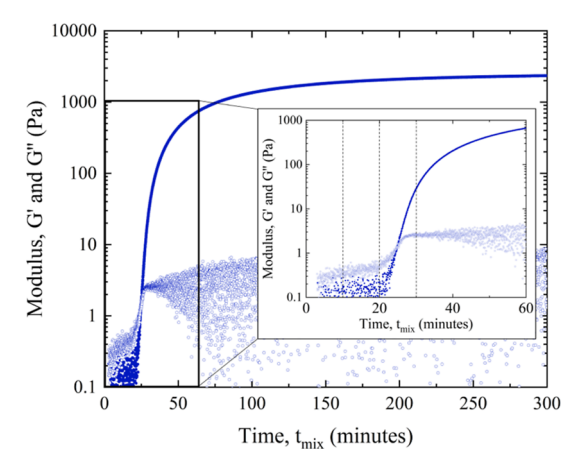


**Figure 2.** Storage modulus (G', closed symbols) and loss modulus (G'', open symbols) during the gelation of a tetra-PEG hydrogel at  $c^*$  for a representative sample. Data acquisition begins at 3 min to account for the time to place samples on the rheometer stage. Inset of time 0 to 60 min focuses on the crossover point of G' and G'',  $t_{\rm gel} = 24.6$  min. Dotted lines denote 10, 20, 30, and 60 min.

changes most dramatically (several orders of magnitude) within the first 60 min.

SPT of QDs. SPT is used to measure the MSD of PEGfunctionalized QDs at four time points during gelation of  $t_{mix}$  = 10, 20, 30 and 60 min. In addition to facilitating solubility of the QDs in water, PEG functionalization also reduces interactions between the probe and the network, which is composed of PEG repeat units. For the time points before  $t_{\rm gel}$  $t_{\text{mix}} = 10$  and 20 min, the QDs exhibit high mobility (Figure 3). For these time points, a diffusion coefficient can be calculated by fitting the linear portion of the ensemble MSD curve (black lines, Figure 3). At  $t_{mix} = 10$  min, the diffusion coefficient from the ensemble average is  $D_{\rm QD,10} = 2.5 \times 10^6 \, \rm nm^2/s$ . As gelation proceeds ( $t_{\text{mix}} = 20 \text{ min}$ ), the diffusion coefficient decreases by over an order of magnitude to  $D_{\text{QD},20} = 8.1 \times 10^4 \text{ nm}^2/\text{s}$ , indicating that even before the gel time,  $t_{\rm gel} \sim 24$  min, the local structure begins to hinder particle dynamics. We attribute this trend to the initial crosslinking of the macromers, which increases the molecular weights of the polymers in solution and therefore increases the overall solution viscosity. Soon after macroscopic gelation ( $t_{\text{mix}} = 30 \text{ min } > t_{\text{gel}}$ ), the mobility of the spherical QDs is further reduced, with most of the particles becoming immobile as represented by the total number of displacements less than 100 nm. This cutoff for immobile and mobile particles is chosen based on two populations of the MSDs at long  $\tau$ , particularly at  $t_{\text{mix}} = 30$  min, and is applied for all other samples. It is important to note that a small population of mobile particles is present at small  $\tau$  before diffusing out of the image focal plane as indicated by mobile particles only being tracked for short times. In contrast, for times much longer than  $t_{gel}$  ( $t_{mix} = 60$  min), particles with a hydrodynamic diameter of 8 nm are fully immobile, indicating that particles are caged within the network structure, even though the network is still slowly evolving as indicated by rheology (Figure 2).

**SPT of QRs.** To study the effect of nanoparticle shape on dynamics, the MSD of PEG-functionalized QRs,  $9 \times 23$  nm, is compared to that of QDs of similar diameters. Figure 3 shows the MSDs of individual QR trajectories at times before ( $t_{\rm mix} = 10$ , 20 min) and after ( $t_{\rm mix} = 30$ , 60 min) macroscopic gelation,  $t_{\rm gel} = 24.6$  min. At  $t_{\rm mix} = 10$  min, the rods have a diffusion

Table 1. Values of G' and G'' at Key Time Points for Particle Tracking Studies<sup>a</sup>

	before $t_{\mathrm{gel}}$		after $t_{ m gel}$		
	$t_{\rm mix} = 10   {\rm min}$	20 min	30 min	60 min	256 min
G' (Pa)	$0.15 \pm 0.14$	$0.08 \pm 0.07$	$34 \pm 5.5$	$670 \pm 1.4$	$2200 \pm 54$
G'' (Pa)	$0.28 \pm 0.18$	$0.36 \pm 0.13$	$3.0 \pm 0.54$	$3.6 \pm 1.8$	$5.1 \pm 3.9$

<sup>&</sup>lt;sup>a</sup>Average values and standard deviations taken from measurements on separate days (n = 2).

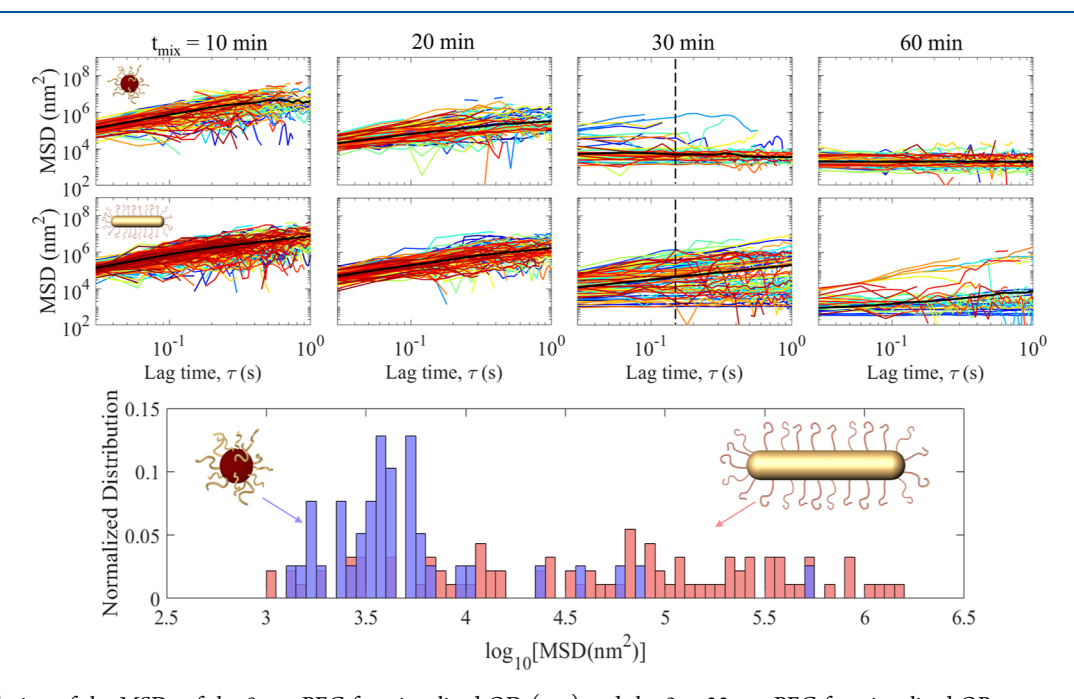


Figure 3. Evolution of the MSDs of the 8 nm PEG-functionalized QD (top) and the  $9 \times 23$  nm PEG-functionalized QR nanoparticles (middle) before ( $t_{\text{mix}} = 10$  and 20 min) and after ( $t_{\text{mix}} = 30$  and 60 min)  $t_{\text{gel}}$ . Black lines are the ensemble average of all particle MSDs. For  $t_{\text{mix}} = 30$  min, the vertical dashed line represents  $\tau = 0.15$  s. Normalized distribution of individual MSDs ( $t_{\text{mix}} = 30$  min) for both QDs (blue) and QRs (red) at a single  $\tau$ ,  $\tau = 0.15$  s (bottom).

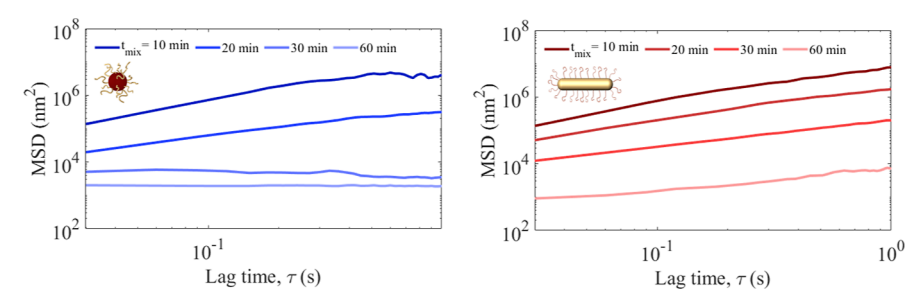


Figure 4. Ensemble average of MSDs as a function of  $\tau$  before ( $t_{\text{mix}} = 10$ , 20 min) and after ( $t_{\text{mix}} = 30$ , 60 min) macroscopic gelation,  $t_{\text{gel}}$ , for QD (left, blue) and QR (right, red).

coefficient of  $2.1 \times 10^6$  nm²/s, slightly lower than the 8 nm QDs at the same  $t_{\rm mix}$ . After 20 min, the diffusion coefficient decreases to  $4.9 \times 10^5$  nm²/s. However, just after  $t_{\rm gel}$  and when  $t_{\rm mix}=30$  min, the individual trajectories exhibit a broad range of MSDs, indicating that individual QRs are exploring disparate local environments. Finally, at times much longer than  $t_{\rm gel}$  ( $t_{\rm mix}=60$  min), the population of immobile, caged particles dominates, while a smaller population of the mobile particle remains with MSD values that are dramatically reduced from those at  $t_{\rm mix}=30$  min.

Comparing the Dynamics of Rods and Spheres. To more easily differentiate between the dynamics of QRs and QDs during gelation, the ensemble MSDs at  $t_{\rm mix} = 10$ , 20, 30 and 60 min are compared as a function of lag time,  $\tau$ , as shown

in Figure 4. At early times ( $t_{\rm mix}=10~{\rm min}$ ), the diffusion coefficient and ensemble MSD of the QDs are larger than that of the QRs. Given the relative hydrodynamic diameters QD (8 nm) and QR (20.5 nm) of the nanoparticles, this difference is consistent with classical models of nanoparticle diffusion because smaller particles are expected to diffuse faster than larger particles if the medium has the same viscosity. However, at times even before  $t_{\rm gel}$ , the rods begin to exhibit increased mobility relative to their spherical counterparts, as can be seen by comparing both the diffusion coefficient and the ensemble MSDs at  $t_{\rm mix}=20~{\rm min}$  (Figure 4). While the dynamics of both the QDs and QRs are reduced compared to the results at  $t_{\rm mix}=10~{\rm min}$ , the diffusion coefficient for the 9 × 23 nm QRs is 5 times larger than the 8 nm QDs in the same local environment.

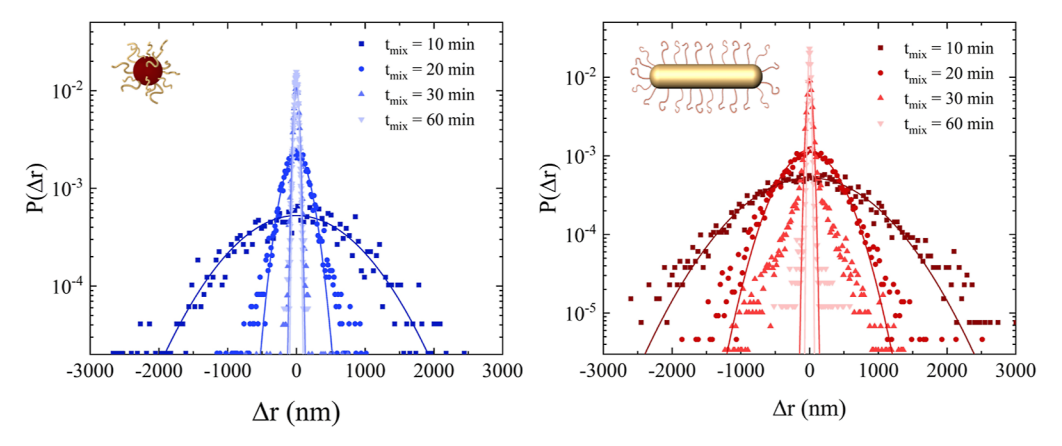


Figure 5. Van Hove distribution functions for various time points during the tetra-PEG gelation process,  $t_{\text{mix}}$  at  $\tau = 0.15$  s, for the QD (left, blue) and QR (right, red) nanoparticles. Lines are Gaussian fits to  $t_{\text{mix}} = 10$ , 20, 30, and 60 min. Y-axis scaling is different between particle types to account for changes in statistics.

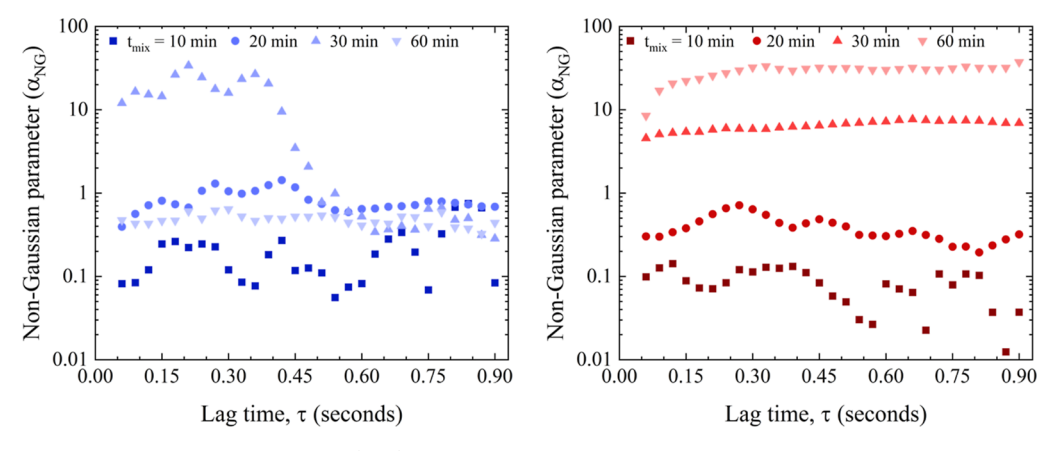


Figure 6. Evolution of the non-Gaussian parameter ( $\alpha_{NG}$ ) at different lag times,  $\tau$ , at increasing times post  $t_{mix} = 0$  min during the tetra-PEG gelation process for the QD (left, blue) and QR (right, red) nanoparticles.

These differences are also observed as the reaction proceeds. For example, at  $t_{\rm mix}=30$  min, the majority of QDs are immobile (Figure 3, top row), whereas a distinct population of the QRs remain mobile (Figure 3, middle row). Finally, at times much longer than  $t_{\rm gel}$ ,  $t_{\rm mix}=60$  min, almost all the QDs are immobilized, whereas some QRs exhibit mobility. This analysis of the individual and ensemble MSDs demonstrates that at times near and after the gel time,  $t_{\rm gel}$ , QRs exhibit enhanced dynamics compared to their spherical counterparts.

To differentiate between mobile and immobile particles, Figure 3 (bottom row) shows the normalized distribution of MSDs for  $t_{\rm mix}=30$  min at  $\tau=0.15$  s, denoted by the dashed line in Figure 3. The  $\tau=0.15$  s time point was chosen to both capture the contribution of the few mobile particles, while also retaining good statistics. For the QRs, the range of particle trajectories at this  $\tau$  can be visualized, where the rods span an MSD range from  $10^3$  to  $10^{6.2}$  nm², over 3 orders of magnitude. Comparatively, while a minority of individual mobile particles can be visualized for the QDs, the majority of the MSDs are clustered around  $10^{3.5}$  nm², indicating that they are immobilized within the network, as shown in Figure 3.

The distribution of particle displacements can be further distinguished by plotting the van Hove distribution function,  $p(\Delta r, \tau)$ , which represents the probability of finding a particle at a given displacement,  $\Delta r$ , at a given  $\tau$ . For monodisperse particles diffusing through a homogeneous fluid, the distribution of particle displacements can be fit to a Gaussian

distribution. However, in heterogeneous matrices, where particles undergo a variety of displacements due to their different local environments, the van Hove distribution function deviates from a Gaussian profile and is characterized by long exponential tails corresponding to low probability, large displacements. In addition, the non-Gaussian parameter,  $\alpha_{\rm NG}$ , provides a quantifiable measure of the deviation of the van Hove distribution from Gaussian behavior. Specifically,  $\alpha_{\rm NG}$  compares the second and fourth moments of the displacements at each lag time,  $\tau$ , as described by the following equation

$$\alpha_{\rm NG} = \frac{\langle \Delta x^4(\tau) \rangle}{3\langle \Delta x^2(\tau) \rangle^2} - 1 \tag{3}$$

If  $\alpha_{\rm NG}$  = 0 for each  $\tau$ , then the displacement increments are Gaussian. Conversely, if  $\alpha_{\rm NG} \neq 0$ , it suggests the presence of heterogeneity.<sup>64</sup>

As seen in Figure 5, although the van Hove distribution function can be fit to a Gaussian at  $t_{\rm mix}=10$  min, the QD displacements at  $t_{\rm mix}=20$  min exhibit these exponential tails before returning to a nearly Gaussian profile at  $t_{\rm mix}=60$  min. Interestingly, for the QRs, the exponential tails are the most pronounced at  $t_{\rm mix}=30$  and 60 min, with approximately Gaussian-shaped displacement probabilities at early times  $t_{\rm mix}=10$  and 20 min. Comparing the van Hove distribution functions for QD and QR at  $t_{\rm mix}=30$  min, the QRs have

distinct exponential tails, whereas the QDs have minimal large displacements. Additionally, for the QR particles, the magnitude of the displacements in the exponential tails clearly increase with  $\tau$ , ( $\tau$  = 0.06, 0.15, and 0.3 s) characteristic of mobile particles experiencing a range of local environments (see Supporting Information).

Figure 6 shows the evolution of  $\alpha_{\rm NG}$  as  $\tau$  increases from 0.06 to 0.9 s during gelation ( $t_{\text{mix}} = 10, 20, 30, 60 \text{ min}$ ) for both the QD and QR nanoparticles. At  $t_{\rm mix}$  = 10 min, the average values of  $\alpha_{\rm NG}$  are relatively low, namely 0.22 and 0.08 for the QDs and QRs, respectively. At early times in gelation, these relatively low values suggest that the spherical and rod particles experience a relatively homogeneous local environment, as shown in Figure 1. Although a percolated network has not yet formed at  $t_{mix} = 20 \text{ min (Figure 2)}$ , the increase in the average  $\alpha_{\rm NG}$  indicates that both types of particles experience a more heterogeneous environment. This behavior correlates with a decrease in the diffusion coefficient consistent with the early signs of gel formation, including regions of a loosely crosslinked network that the particles can explore. For the QDs at  $t_{\rm mix}$  = 30 min,  $\alpha_{\rm NG}$  is initially high at early  $\tau$  but decreases abruptly at  $\tau = 0.33$ . The observed decrease is attributed to the mobile QDs diffusing out of the plane of imaging and being tracked for short times, only up to  $\tau = 0.45$  s. Furthermore, the change in the slope of ensemble MSD at  $t_{mix}$  also reflects the contribution of the immobile particles at long times. 14 Thus, at small  $\tau$ , both mobile and immobile populations contribute to  $\alpha_{\rm NG}$ , whereas for  $\tau > 0.45$  s, only immobile QDs contribute, resulting in a lower value due to the homogeneity of the local environment for the caged QDs. At long times,  $t_{mix} = 60$  min, all QDs are immobile resulting in a decrease in  $\alpha_{NG}$ , with an average  $\alpha_{\rm NG}$  of 0.48. By comparison, for the QRs, the average value of  $\alpha_{NG}$  continues to increase monotonically from  $t_{mix}$  = 10, 20, 30, and 60 min as gelation proceeds. Unlike their QD counterparts, the average value of  $\alpha_{NG}$  for the QRs continues to increase from 30 to 60 min. This trend is consistent with QRs retaining some mobility late in network formation, as can be seen in the large displacements in Figure 5. In summary, van Hove analysis suggests at short and intermediate times of gelation that the QDs experience more heterogeneous dynamics compared to the QRs. However, at later times, the QRs experience more heterogeneous dynamics after the onset of a percolated network at  $t_{\rm gel}$ .

The mechanism of nanorod dynamics can be understood by following the trajectory of individual QRs. Along with the increased percentage of mobile particles and faster dynamics, mobile QR particles are also observed to undergo repeated caging followed by longer displacements. A sample trajectory is shown in Figure 7 where the particle at t = 0 s starts at X = Y = 00 (dark blue). During the initial 1.8 s (dark blue), the probe moves more than 2  $\mu$ m, before becoming immobilized in a small region (lighter blue), less than a hundred nanometers in size, denoted by a open black circle. The size of the cage reflects both the resolution of the instrument (~10 s nm) and fluctuations of the local network surrounding the caged particle. The particle then leaves the cage at 4.38 s, before undergoing another larger displacement ( $\sim 1 \mu m$ ) before becoming caged once more at 7.53 s (green and yellow). Figure 7 shows a single trajectory of a QR that remains within the imaging plane for up to 12 s, allowing for the repeated caging and mobile trajectories to be easily visualized. This caging to mobile transition is observed for multiple QR trajectories, as shown in Supporting Information.

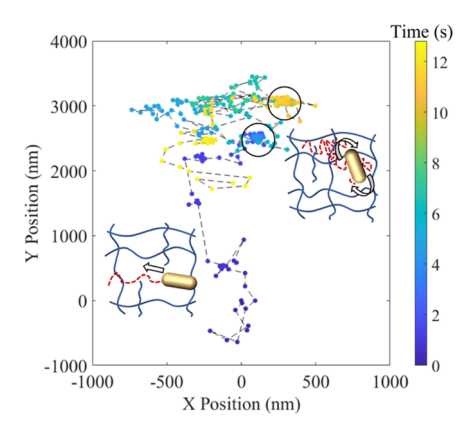


**Figure 7.** Representative single trajectory of a QR nanoparticle showing large displacements and caging in a tetra-PEG hydrogel at 30 min into the gelation process. The origin is located at X=Y=0. The trajectory is followed for 12.8 s as the colors change from blue  $(0\ s)$  to yellow  $(12.8\ s)$ . The open black circles indicate regions of probe caging, where the QR spends an extended period of time (over a second) in a confined region of the gel as represented in the schematic in the upper right. Large displacements are also observed as represented in the schematic in the lower left.

Our findings can be compared with two studies that have observed enhanced rod dynamics in biopolymer networks. In particular, we focus on the divergent QD and QR dynamics after  $t_{gel}$  and the presence of caging to mobile behavior. As previously detailed in the introduction, multiple studies have previously investigated rod dynamics in similar systems. For example, Yu et al. compared the dynamics of silica spheres and rods in mucus and via molecular dynamics simulations.<sup>39</sup> Moreover, Lee et al. examined the infiltration of TMV and CPMV into agarose spheroids. 41 Taken together, these studies similarly demonstrated that rod-shaped particles exhibit enhanced dynamics and mobility in confined networks when compared to their spherical counterparts. We propose that our system of PEG-functionalized QRs ( $9 \times 23$  nm) exhibit similar behaviors as these studies due to the heterogeneity of the hydrogel network during the gelation process. In addition to these mechanisms, we also investigated if the QRs disrupted the tetra-PEG network during gelation, as measured via rheology, in which we found minimal changes in macroscopic properties suggesting that this was not the primary mechanism of changes in dynamics (see Supporting Information).

A unique characteristic of the mobile QR trajectories is the observation of intermittent caging followed by longer displacements in the hydrogel structures formed soon after the gel time, namely  $t_{\rm mix}$  = 30 min. In the work of Yu et al., increased rod mobility was attributed to the rotational component of the rod dynamics, which allows the particle to rotate around a polymer chain when the rod length is similar to  $\xi$ .<sup>39</sup> In our experimental system, this would correspond to  $\xi\sim$  23 nm. While the final average mesh size of the tetra-PEG hydrogel is much smaller, with  $\xi \sim 3$  nm, at times after the gel time ( $t_{\rm mix}$  = 30 min), the network is likely much more open and heterogeneous, as indicated by the low storage modulus G'~ 30 Pa and heterogeneous particle dynamics, respectively.<sup>53</sup> At these intermediate times, a range of mesh sizes would be expected across the hydrogel structure that span the diameter and length of the QR. We hypothesize that the ability of a single rod particle to move from a caged to mobile state can be attributed to the rod rotational dynamics, allowing the rods to

tilt and then move out of a region of more dense crosslinking and into more open network areas more easily than their spherical counterparts.

One notable aspect of the trajectory in Figure 7 is the large displacement of the individual QR. The observed displacements between caging events can be attributed to the increased parallel diffusion, similar to that observed for the TMV infiltrating into agarose spheroids.<sup>41</sup> In this previous work, the authors hypothesized that the initial increased infiltration of TMV into agarose may be attributed to the TMV particles aligning along their long axis within the pore structure. Interestingly, the authors also attribute the reduction in rod infiltration at longer times to the trapping of rods that block subsequent TMV infiltration. Our experiments do not show this behavior because of the low concentrations of particles used in SPT compared to the large concentrations required for bulk fluorescence measurements. Overall, we attribute the rod's ability to exit caged regions to rod tilting due to particle anisotropy, and the large displacements between caging events to increased parallel diffusion along the rod axis in the more open network. Figure 7 shows a schematic of the nanorods exhibiting the caged and mobile behavior.

Although they do not exhibit the caged to mobile behavior visualized with the QRs, QDs do exhibit limited mobility in the hydrogel structures after the gel time, namely at  $t_{\rm mix}=30$  min. While the majority of the QDs are immobile, as indicated by the ensemble average and distribution of displacements in Figure 4, there are a few fast moving particles that rapidly diffuse out of the plane of imaging. This observation suggests that those QDs are experiencing regions of low confinement and therefore open network regions, which allows for rapid dynamics. Conversely, a large population of particles are localized on the order of the resolution of the instrument ( $\sim 10$ 's nm). Because QDs are unable to undergo rotational dynamics that contribute to their mobility, the immobile particles remain trapped, at least on the time scale of imaging.<sup>39</sup>

The proposed mechanism of QRs rotating out of confining cages to enhance dynamics would greatly benefit from both computational and experimental studies. In particular, additional experiments that specifically track the rotational dynamics of the rod would be useful in further understanding rod dynamics. Examples of SPT techniques capable of tracking rod dynamics include polarized total internal reflection fluorescence microscopy<sup>65</sup> for QRs and laser-illuminated dark-field microscopy for gold nanorods.<sup>66</sup> Additional molecular dynamics simulations, similar to those conducted by Yu et al., but in heterogeneous hydrogel structures to mimic the structures present throughout the gelation process would be useful.<sup>39</sup> Overall, examining rotational dynamics during caged periods and the transition to mobile behavior in both computational and experimental studies could further elucidate the impact of rotational dynamics on rod behavior.

#### CONCLUSIONS

In this study, the dynamics of PEG-functionalized QDs and QRs are examined during the gelation process of a tetra-PEG hydrogel. Changes in macroscopic hydrogel properties during gelation such as  $t_{\rm gel}$  were determined via rheological measurements of the tetra-PEG hydrogels. During the initial stages of gelation, before  $t_{\rm gel}$ , the QDs exhibit faster dynamics than the QRs due to their smaller hydrodynamic diameter. At intermediate gelation times (before and after  $t_{\rm gel}$ ), the QRs

exhibit faster particle dynamics than the QDs. At times just after  $t_{gel}$ , QRs exhibit a range of particle mobility, including completely immobile particles, as well as particles that can escape localized cages and diffuse large distances. Comparisons to previous work on rod particle dynamics elucidate potential mechanisms for the caging to mobile behavior of the QR particles, including the rotational dynamics of the QRs and their increased parallel diffusion in confining polymeric matrices. Future work measuring the rotational dynamics of QRs in the evolving tetra-PEG structures could be used to potentially validate the proposed mechanisms underlying enhanced QR dynamics during gelation. In all, this study serves as an investigation of the influence of particle shape anisotropy in a model tetra-PEG hydrogel system on nanoparticle dynamics; it is expected that these insights on the enhancement of rod particle dynamics will prove to be useful toward the use of rod nanoparticles in a range of biomedical applications, including drug delivery.

#### ASSOCIATED CONTENT

## **5** Supporting Information

The Supporting Information is available free of charge at https://pubs.acs.org/doi/10.1021/acs.macromol.2c01577.

Characterization of QDs and QRs (TEM and SPT), rheology of rod-containing networks, additional van Hove distributions, and sample single particle trajectories (PDF)

### AUTHOR INFORMATION

## **Corresponding Authors**

Daeyeon Lee – Department of Chemical and Biomolecular Engineering, University of Pennsylvania, Philadelphia, Pennsylvania 19104, United States; oorcid.org/0000-0001-6679-290X; Email: daeyeon@seas.upenn.edu

Russell J. Composto — Department of Chemical and Biomolecular Engineering, Department of Materials Science and Engineering, and Department of Bioengineering, University of Pennsylvania, Philadelphia, Pennsylvania 19104, United States; orcid.org/0000-0002-5906-2594; Email: composto@seas.upenn.edu

#### Authors

Katie A. Rose — Department of Chemical and Biomolecular Engineering, University of Pennsylvania, Philadelphia, Pennsylvania 19104, United States; orcid.org/0000-0001-7500-3108

Natalie Gogotsi — Department of Materials Science and Engineering, University of Pennsylvania, Philadelphia, Pennsylvania 19104, United States

Jonathan H. Galarraga – Department of Bioengineering, University of Pennsylvania, Philadelphia, Pennsylvania 19104, United States; orcid.org/0000-0002-1146-5941

Jason A. Burdick — Department of Bioengineering, University of Pennsylvania, Philadelphia, Pennsylvania 19104, United States; BioFrontiers Institute and Department of Chemical and Biological Engineering, University of Colorado, Boulder, Colorado 80309, United States; orcid.org/0000-0002-2006-332X

Christopher B. Murray — Department of Materials Science and Engineering and Department of Chemistry, University of Pennsylvania, Philadelphia, Pennsylvania 19104, United States Complete contact information is available at: https://pubs.acs.org/10.1021/acs.macromol.2c01577

#### Notes

The authors declare no competing financial interest.

#### ACKNOWLEDGMENTS

The authors thank Dr. Matthew Brukman for instrument support in the Singh Center for Nanotechnology, Professor Matteo Cargnello for providing CdSe/ZnS QDs, and Professor Ryan Poling-Skutvik for valuable conversation and insights. Support was provided by the NSF-PIRE-OISE-1545884 (R.J.C., D.L., C.B.M., N.G., K.A.R.), NSF Graduate Fellowships (K.A.R., J.H.G.), NSF-POLYMERS-DMR-1905912 (R.J.C.), NSF-MRSEC-DMR 1720530 (N.G., C.B.M., D.L., J.A.B.), and NSF-CBET-2034122 (R.J.C.). Particle tracking experiments were performed at the Scanning and Local Probe Facility at the Singh Center for Nanotechnology at the University of Pennsylvania, supported by NSF-MRSEC-DMR-1720530.

## REFERENCES

- (1) Ozay, O.; Ekici, S.; Baran, Y.; Kubilay, S.; Aktas, N.; Sahiner, N. Utilization of Magnetic Hydrogels in the Separation of Toxic Metal Ions from Aqueous Environments. *Desalination* **2010**, 260, 57–64.
- (2) Getachew, B. A.; Kim, S.-R.; Kim, J.-H. Self-Healing Hydrogel Pore-Filled Water Filtration Membranes. *Environ. Sci. Technol.* **2017**, *51*, 905–913.
- (3) Kar-On Leung, B.; Robinson, G. Ultrafiltration through Hydrogels: Effects of Hydration and Crosslinking. *J. Membr. Sci.* **1990**, *52*, 1–18.
- (4) Cussler, E. L.; Stokar, M. R.; Varberg, J. E. Gels as Size Selective Extraction Solvents. *AIChE J.* **1984**, *30*, 578–582.
- (5) Park, C. H.; Orozco-Avila, I. Concentrating Cellulases from Fermented Broth Using a Temperature-Sensitive Hydrogel. *Biotechnol. Prog.* **1992**, *8*, 521.
- (6) Maguire, S. M.; Boyle, M. J.; Bilchak, C. R.; Demaree, J. D.; Keller, A. W.; Krook, N. M.; Ohno, K.; Kagan, C. R.; Murray, C. B.; Rannou, P.; Composto, R. J. Grafted Nanoparticle Surface Wetting during Phase Separation in Polymer Nanocomposite Films. ACS Appl. Mater. Interfaces 2021, 13, 37628–37637.
- (7) Bailey, E. J.; Winey, K. I. Dynamics of Polymer Segments, Polymer Chains, and Nanoparticles in Polymer Nanocomposite Melts: A Review. *Prog. Polym. Sci.* **2020**, *105*, 101242.
- (8) Kalathi, J. T.; Yamamoto, U.; Schweizer, K. S.; Grest, G. S.; Kumar, S. K. Nanoparticle Diffusion in Polymer Nanocomposites. *Phys. Rev. Lett.* **2014**, *112*, 108301.
- (9) Medidhi, K. R.; Padmanabhan, V. Diffusion of Polymer-Grafted Nanoparticles in a Homopolymer Matrix. *J. Chem. Phys.* **2019**, *150*, 044905.
- (10) Karatrantos, A.; Clarke, N.; Composto, R. J.; Winey, K. I. Structure, Entanglements and Dynamics of Polymer Nanocomposites Containing Spherical Nanoparticles. *IOP Conf. Ser.: Mater. Sci. Eng.* **2014**, *64*, 012041.
- (11) Wang, Y.; Wang, J.; Yuan, Z.; Han, H.; Li, T.; Li, L.; Guo, X. Chitosan Cross-Linked Poly(Acrylic Acid) Hydrogels: Drug Release Control and Mechanism. *Colloids Surf., B* **2017**, *152*, 252–259.
- (12) Matricardi, P.; Di Meo, C.; Coviello, T.; Hennink, W. E.; Alhaique, F. Interpenetrating Polymer Networks Polysaccharide Hydrogels for Drug Delivery and Tissue Engineering. *Adv. Drug Delivery Rev.* **2013**, *65*, 1172–1187.
- (13) Parrish, E.; Caporizzo, M. A.; Composto, R. J. Network Confinement and Heterogeneity Slows Nanoparticle Diffusion in Polymer Gels. *J. Chem. Phys.* **2017**, *146*, 203318.
- (14) Lee, C. H.; Crosby, A. J.; Emrick, T.; Hayward, R. C. Characterization of Heterogeneous Polyacrylamide Hydrogels by

- Tracking of Single Quantum Dots. Macromolecules 2014, 47, 741-749
- (15) Hansing, J.; Ciemer, C.; Kim, W. K.; Zhang, X.; DeRouchey, J. E.; Netz, R. R. Nanoparticle Filtering in Charged Hydrogels: Effects of Particle Size, Charge Asymmetry and Salt Concentration. *Eur. Phys. J. E: Soft Matter Biol. Phys.* **2016**, *39*, 53.
- (16) Parrish, E.; Seeger, S. C.; Composto, R. J. Temperature-Dependent Nanoparticle Dynamics in Poly(N-isopropylacrylamide) Gels. *Macromolecules* **2018**, *51*, 3597–3607.
- (17) Rose, K. A.; Lee, D.; Composto, R. J. pH-Mediated Nanoparticle Dynamics in Hydrogel Nanocomposites. *Soft Matter* **2021**, *17*, 2765–2774.
- (18) Zhang, X.; Hansing, J.; Netz, R. R.; DeRouchey, J. E. Particle Transport through Hydrogels Is Charge Asymmetric. *Biophys. J.* **2015**, *108*, 530–539.
- (19) Hansing, J.; Duke, J. R.; Fryman, E. B.; DeRouchey, J. E.; Netz, R. R. Particle Diffusion in Polymeric Hydrogels with Mixed Attractive and Repulsive Interactions. *Nano Lett.* **2018**, *18*, 5248–5256.
- (20) Hansing, J.; Netz, R. R. Hydrodynamic Effects on Particle Diffusion in Polymeric Hydrogels with Steric and Electrostatic Particle-Gel Interactions. *Macromolecules* **2018**, *51*, 7608–7620.
- (21) Park, J.; Bailey, E. J.; Composto, R. J.; Winey, K. I. Single-Particle Tracking of Nonsticky and Sticky Nanoparticles in Polymer Melts. *Macromolecules* **2020**, *53*, 3933–3939.
- (22) Smith, M.; Poling-Skutvik, R.; Slim, A. H.; Willson, R. C.; Conrad, J. C. Dynamics of Flexible Viruses in Polymer Solutions. *Macromolecules* **2021**, *54*, 4557–4563.
- (23) Molaei, M.; Atefi, E.; Crocker, J. C. Nanoscale Rheology and Anisotropic Diffusion Using Single Gold Nanorod Probes. *Phys. Rev. Lett.* **2018**, *120*, 118002.
- (24) Choi, J.; Cargnello, M.; Murray, C. B.; Clarke, N.; Winey, K. I.; Composto, R. J. Fast Nanorod Diffusion through Entangled Polymer Melts. *ACS Macro Lett.* **2015**, *4*, 952–956.
- (25) Wang, J.; O'Connor, T. C.; Grest, G. S.; Zheng, Y.; Rubinstein, M.; Ge, T. Diffusion of Thin Nanorods in Polymer Melts. *Macromolecules* **2021**, *54*, 7051–7059.
- (26) Kim, M. J.; Cho, H. W.; Kim, J.; Kim, H.; Sung, B. J. Translational and Rotational Diffusion of a Single Nanorod in Unentangled Polymer Melts. *Phys. Rev. E: Stat., Nonlinear, Soft Matter Phys.* **2015**, 92, 042601.
- (27) Alam, S.; Mukhopadhyay, A. Translational and Rotational Diffusions of Nanorods within Semidilute and Entangled Polymer Solutions. *Macromolecules* **2014**, *47*, 6919–6924.
- (28) Karatrantos, A.; Composto, R. J.; Winey, K. I.; Clarke, N. Nanorod Diffusion in Polymer Nanocomposites by Molecular Dynamics Simulations. *Macromolecules* **2019**, *52*, 2513–2520.
- (29) Lin, R. D.; Steinmetz, N. F. Tobacco Mosaic Virus Delivery of Mitoxantrone for Cancer Therapy. *Nanoscale* **2018**, *10*, 16307–16313.
- (30) Pitek, A. S.; Hu, H.; Shukla, S.; Steinmetz, N. F. Cancer Theranostic Applications of Albumin-Coated Tobacco Mosaic Virus Nanoparticles. *ACS Appl. Mater. Interfaces* **2018**, *10*, 39468–39477.
- (31) Shukla, S.; Marks, I.; Church, D.; Chan, S.-K.; Pokorski, K.; Steinmetz, F. Tobacco Mosaic Virus for the Targeted Delivery of Drugs to Cells Expressing Prostate-Specific Membrane Antigen. *RSC Adv.* **2021**, *11*, 20101–20108.
- (32) Le, D. H. T.; Lee, K. L.; Shukla, S.; Commandeur, U.; Steinmetz, N. F. Potato Virus X, a Filamentous Plant Viral Nanoparticle for Doxorubicin Delivery in Cancer Therapy. *Nanoscale* **2017**, *9*, 2348–2357.
- (33) Shukla, S.; DiFranco, N. A.; Wen, A. M.; Commandeur, U.; Steinmetz, N. F. To Target or Not to Target: Active vs. Passive Tumor Homing of Filamentous Nanoparticles Based on Potato Virus X. Cell. Mol. Bioeng. 2015, 8, 433–444.
- (34) Shukla, S.; Roe, A. J.; Liu, R.; Veliz, F. A.; Commandeur, U.; Wald, D. N.; Steinmetz, N. F. Affinity of Plant Viral Nanoparticle Potato Virus X (PVX) towards Malignant B Cells Enables Cancer Drug Delivery. *Biomater. Sci.* **2020**, *8*, 3935–3943.

- (35) Choi, W. I.; Kim, J.-Y.; Kang, C.; Byeon, C. C.; Kim, Y. H.; Tae, G. Tumor Regression In Vivo by Photothermal Therapy Based on Gold-Nanorod-Loaded, Functional Nanocarriers. *ACS Nano* **2011**, *5*, 1995–2003.
- (36) Agarwal, A.; Huang, S. W.; O'Donnell, M.; Day, K. C.; Day, M.; Kotov, N.; Ashkenazi, S. Targeted Gold Nanorod Contrast Agent for Prostate Cancer Detection by Photoacoustic Imaging. *J. Appl. Phys.* **2007**, *102*, 064701.
- (37) Venkatesan, R.; Pichaimani, A.; Hari, K.; Balasubramanian, P. K.; Kulandaivel, J.; Premkumar, K. Doxorubicin Conjugated Gold Nanorods: A Sustained Drug Delivery Carrier for Improved Anticancer Therapy. *J. Mater. Chem. B* **2013**, *1*, 1010–1018.
- (38) Banerjee, A.; Qi, J.; Gogoi, R.; Wong, J.; Mitragotri, S. Role of Nanoparticle Size, Shape and Surface Chemistry in Oral Drug Delivery. *J. Controlled Release* **2016**, 238, 176–185.
- (39) Yu, M.; Wang, J.; Yang, Y.; Zhu, C.; Su, Q.; Guo, S.; Sun, J.; Gan, Y.; Shi, X.; Gao, H. Rotation-Facilitated Rapid Transport of Nanorods in Mucosal Tissues. *Nano Lett.* **2016**, *16*, 7176–7182.
- (40) Chauhan, V. P.; Popović, Z.; Chen, O.; Cui, J.; Fukumura, D.; Bawendi, M. G.; Jain, R. K. Fluorescent Nanorods and Nanospheres for Real-Time in Vivo Probing of Nanoparticle Shape-Dependent Tumor Penetration. *Angew. Chem., Int. Ed.* **2011**, *50*, 11417–11420.
- (41) Lee, K. L.; Hubbard, L. C.; Hern, S.; Yildiz, I.; Gratzl, M.; Steinmetz, N. F. Shape Matters: The Diffusion Rates of TMV Rods and CPMV Icosahedrons in a Spheroid Model of Extracellular Matrix Are Distinct. *Biomater. Sci.* **2013**, *1*, 581–588.
- (42) Nishi, K.; Chijiishi, M.; Katsumoto, Y.; Nakao, T.; Fujii, K.; Chung, U.-i.; Noguchi, H.; Sakai, T.; Shibayama, M. Rubber Elasticity for Incomplete Polymer Networks. *J. Chem. Phys.* **2012**, *137*, 224903.
- (43) Akagi, Y.; Katashima, T.; Sakurai, H.; Chung, U.-i.; Sakai, T. Ultimate Elongation of Polymer Gels with Controlled Network Structure. *RSC Adv.* **2013**, *3*, 13251.
- (44) Akagi, Y.; Sakurai, H.; Gong, J. P.; Chung, U.-i.; Sakai, T. Fracture Energy of Polymer Gels with Controlled Network Structures. *J. Chem. Phys.* **2013**, *139*, 144905.
- (45) Sakai, T.; Akagi, Y.; Kondo, S.; Chung, U. Experimental Verification of Fracture Mechanism for Polymer Gels with Controlled Network Structure. *Soft Matter* **2014**, *10*, 6658–6665.
- (46) Lin, T.-S.; Wang, R.; Johnson, J. A.; Olsen, B. D. Topological Structure of Networks Formed from Symmetric Four-Arm Precursors. *Macromolecules* **2018**, *51*, 1224–1231.
- (47) Lange, F.; Schwenke, K.; Kurakazu, M.; Akagi, Y.; Chung, U.-i.; Lang, M.; Sommer, J.-U.; Sakai, T.; Saalwächter, K. Connectivity and Structural Defects in Model Hydrogels: A Combined Proton NMR and Monte Carlo Simulation Study. *Macromolecules* **2011**, *44*, 9666–9674.
- (48) Sakai, T. Gelation Mechanism and Mechanical Properties of Tetra-PEG Gel. *React. Funct. Polym.* **2013**, 73, 898–903.
- (49) Shibayama, M.; Li, X.; Sakai, T. Precision polymer network science with tetra-PEG gels-a decade history and future. *Colloid Polym. Sci.* **2019**, 297, 1–12.
- (50) Kurakazu, M.; Katashima, T.; Chijiishi, M.; Nishi, K.; Akagi, Y.; Matsunaga, T.; Shibayama, M.; Chung, U.-i.; Sakai, T. Evaluation of Gelation Kinetics of Tetra-PEG Gel. *Macromolecules* **2010**, *43*, 3935—3940.
- (51) Tsuji, Y.; Li, X.; Shibayama, M. Evaluation of Mesh Size in Model Polymer Networks Consisting of Tetra-Arm and Linear Poly(Ethylene Glycol)s. *Gels* **2018**, *4*, 50.
- (52) Nishi, K.; Fujii, K.; Katsumoto, Y.; Sakai, T.; Shibayama, M. Kinetic Aspect on Gelation Mechanism of Tetra-PEG Hydrogel. *Macromolecules* **2014**, *47*, 3274–3281.
- (53) Matsunaga, T.; Sakai, T.; Akagi, Y.; Chung, U. I.; Shibayama, M. Structure Characterization of Tetra-PEG Gel by Small-Angle Neutron Scattering. *Macromolecules* **2009**, *42*, 1344–1351.
- (54) Parrish, E.; Rose, K. A.; Cargnello, M.; Murray, C. B.; Lee, D.; Composto, R. J. Nanoparticle Diffusion during Gelation of Tetra Poly(Ethylene Glycol) Provides Insight into Nanoscale Structural Evolution. *Soft Matter* **2020**, *16*, 2256–2265.

- (55) Cargnello, M.; Diroll, B. T.; Gaulding, E. A.; Murray, C. B. Enhanced Energy Transfer in Quasi-Quaternary Nanocrystal Superlattices. *Adv. Mater.* **2014**, *26*, 2419–2423.
- (56) Diroll, B. T.; Turk, M. E.; Gogotsi, N.; Murray, C. B.; Kikkawa, J. M. Ultrafast Photoluminescence from the Core and the Shell in CdSe/CdS Dot-in-Rod Heterostructures. *ChemPhysChem* **2016**, *17*, 759–765.
- (57) Diroll, B. T.; Gogotsi, N.; Murray, C. B. Statistical Description of CdSe/CdS Dot-in-Rod Heterostructures Using Scanning Transmission Electron Microscopy. *Chem. Mater.* **2016**, *28*, 3345–3351.
- (58) Tirado, M.; Martínez, C.; de la Torre, J. Comparison of Theories for the Translational and Rotational Diffusion Coefficients of Rod-like Macromolecules. Application to Short DNA Fragments. *J. Chem. Phys.* **1984**, *81*, 2047–2052.
- (59) Matsunaga, T.; Sakai, T.; Akagi, Y.; Chung, U. I.; Shibayama, M. SANS and SLS Studies on Tetra-Arm PEG Gels in as-Prepared and Swollen States. *Macromolecules* **2009**, 42, 6245–6252.
- (60) Ruhnow, F.; Zwicker, D.; Diez, S. Tracking Single Particles and Elongated Filaments with Nanometer Precision. *Biophys. J.* **2011**, *100*, 2820–2828.
- (61) Rose, K. A.; Molaei, M.; Boyle, M. J.; Lee, D.; Crocker, J. C.; Composto, R. J. Particle Tracking of Nanoparticles in Soft Matter. *J. Appl. Phys.* **2020**, *127*, 191101.
- (62) Tarantino, N.; Tinevez, J.-Y.; Crowell, E. F.; Boisson, B.; Henriques, R.; Mhlanga, M.; Agou, F.; Israël, A.; Laplantine, E. TNF and IL-1 Exhibit Distinct Ubiquitin Requirements for Inducing NEMO–IKK Supramolecular Structures. *J. Cell Biol.* **2014**, 204, 231–245.
- (63) Rahman, A. Correlations in the Motion of Atoms in Liquid Argon. *Phys. Rev.* **1964**, *136*, A405–A411.
- (64) Kegel, W. K.; van Blaaderen, a. A. Direct Observation of Dynamical Heterogeneities in Colloidal Hard-Sphere Suspensions. *Science* **2000**, 287, 290–293.
- (65) Beausang, J. F.; Shroder, D. Y.; Nelson, P. C.; Goldman, Y. E. Tilting and Wobble of Myosin V by High-Speed Single-Molecule Polarized Fluorescence Microscopy. *Biophys. J.* **2013**, *104*, 1263–1273.
- (66) Molaei, M.; Sheng, J. Imaging Bacterial 3D Motion Using Digital In-Line Holographic Microscopy and Correlation-Based de-Noising Algorithm. *Opt. Express* **2014**, *22*, 32119–32137.